Operating Wind Power Plants Under Weak Grid Conditions Considering Voltage Stability Constraints

Torsten Lund, Heng Wu, *Member, IEEE*, Hamid Soltani, *Member, IEEE*, John Godsk Nielsen, Gert Karmisholt Andersen, and Xiongfei Wang, *Senior Member, IEEE*

***Abstract*—This article analyzes the power transfer limit (P_{max}) of wind power plants (WPPs) under the weak grid condition. It is pointed out that the impact of different grid parameters and grid configurations on P_{max} cannot be fully reflected by the short-circuit ratio (SCR), but can be readily captured by voltage sensitivity ($\partial Q/\partial V$). Hence, $\partial Q/\partial V$ turns out to be a more appropriate metric for the assessment of P_{max} compared with the SCR. Based on this insight, the voltage control of the WPP is suggested to be implemented at the bus with the highest $\partial Q/\partial V$ to maximize the power transfer capability. Moreover, a dynamic voltage control is further added at the turbine level to improve the disturbance rejection capability of the WPP as well as its dynamic robustness against grid strength variations. Finally, simulation and field test results are given to demonstrate the theoretical analysis and the effectiveness of the proposed control method.**

***Index Terms*—Control, power transfer capacity, stability, voltage sensitivity, weak grid, wind power plants (WPPs).**

I. Introduction

WIND power plants (WPPs) are usually located far away from load centers and synchronous generators with long transmission lines in between, which forms a weak grid at the connection point of the WPP. Hence, operating the WPP stably under the weak grid conditions while maximizing its output power is one of the main concerns for transmission system operators (TSOs) as well as converter manufactures [1], [2].

The WPP with grid-following control can be modeled as a PQ source [3], and the maximum active power transfer (P_{max}) of the WPP is constrained by the angle stability limit ($\partial P/\partial\theta>0$) and the voltage stability limit ($\partial Q/\partial V>0$) [4], [5]. Since both $\partial P/\partial\theta$ and $\partial Q/\partial V$ are affected by the grid strength that is quantified by the short-circuit ratio (SCR), the SCR becomes a widely adopted metric to assess the P_{max} of converter-based generation units like WPPs [3], [6]–[9]. For example, the SCR of the power grid in Panhandle area, Texas, USA, would be monitored by the Electric Reliability Council of Texas (ERCOT) in real-time, and the output power of the WPP in Panhandle area needs to be curtailed if the SCR drops below 1.5 [10]. Yet, this SCR-based metric neglects other factors that would affect $\partial P/\partial\theta$ and $\partial Q/\partial V$ and, hence, might lead to the inaccurate prediction of P_{max} in some scenarios [6]. For example, it is revealed in [11] that $\partial P/\partial\theta$ is also affected by the grid impedance angle (X/R ratio). Hence, different P_{max} of WPPs might be yielded under different X/R ratios, even if the SCR of the grid is the same. Another example given in [12] highlights that P_{max} of WPPs is also affected by the existence of local loads, which, however, cannot be captured in the SCR-based metric either [12].

While there is increasing awareness of shortcomings of SCR-based P_{max} assessment, very little attempt can be found in identifying a more appropriate metric for assessing P_{max} of converter-based generation units like WPPs. To fill this void, this article derives the analytical representation of $\partial P/\partial\theta$ and $\partial Q/\partial V$, based on which, it is revealed that not only grid parameters (X/R ratio, voltage level, etc.), but also grid configurations (presence of local loads, synchronous condenser, etc.), would affect the value of $\partial P/\partial\theta$ and $\partial Q/\partial V$. As will be illustrated in this article, the SCR-based P_{max} assessment would lead to either too optimistic or too pessimistic predictions in these scenarios. Yet, instead of evaluating both $\partial P/\partial\theta$ and $\partial Q/\partial V$ for a more accurate P_{max} assessment, this article reveals that it is generally enough to check $\partial Q/\partial V$ only, as $\partial Q/\partial V$ imposes a stricter constraint on P_{max} than $\partial P/\partial\theta$. Hence, $\partial Q/\partial V$ can be adopted as a more appropriate metric for P_{max} assessment compared with the SCR.

The $\partial Q/\partial V$ metric only identifies the theoretical maximum active power transfer constraint imposed by the ac system. On top of that, the WPP control should be further optimized to enable its operation close to this theoretical limit. The control of the WPP includes the power plant controller (PPC) and individual wind turbine (WT) converter control [13], [14]. In recent years, much research effort has been devoted to optimizing controller parameters of the WT converter to enhance its stability under weak grid conditions [15]–[18]. The general design guideline indicates that lowering the bandwidth of the dc-link voltage control (DVC) loop and the phase-locked loop (PLL) [15]–[17],

Manuscript received 23 March 2022; revised 17 June 2022; accepted 23 July 2022. Date of publication 8 August 2022; date of current version 6 September 2022. Recommended for publication by Associate Editor F. Lin. *(Corresponding author: Heng Wu.)*

Torsten Lund, Hamid Soltani, John Godsk Nielsen, and Gert Karmisholt Andersen are with Vestas Wind Systems, 8100 Aarhus, Denmark (e-mail: tolud@vestas.com; hasol@vestas.com; jogn@vestas.com; gekan@vestas.com).

Heng Wu and Xiongfei Wang are with AAU Energy, Aalborg University, 9220 Aalborg, Denmark (e-mail: hew@energy.aau.dk; xwa@energy.aau.dk).

Color versions of one or more figures in this article are available at https://doi.org/10.1109/TPEL.2022.3197308.

Digital Object Identifier 10.1109/TPEL.2022.3197308

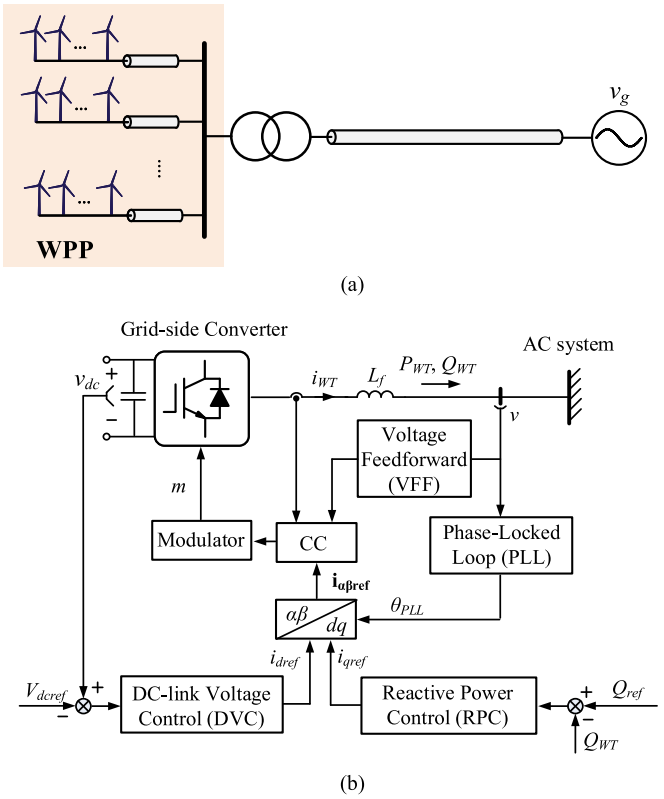

Fig. 1. WPP. (a) Typical configuration. (b) Single-line diagram of the grid-side converter (GSC) of the WT with grid-following control.

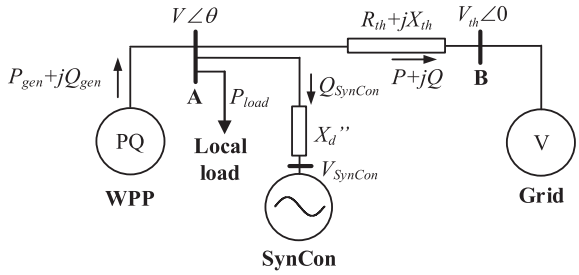

Fig. 2. Equivalent WPP-grid system.

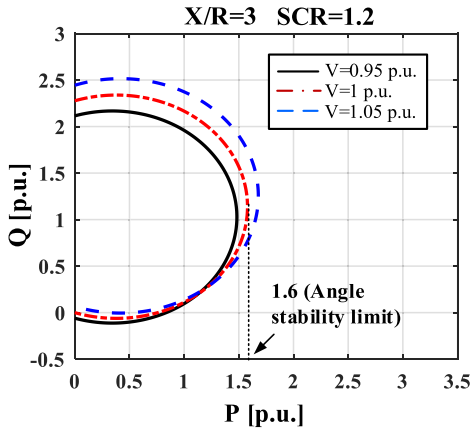

Fig. 3. P-Q curve of the system with X/R = 3, SCR = 1.2, V_{th} = 1 p.u.

as well as increasing the bandwidth of the current control (CC) loop [18], help to stabilize the WT converter under the weak grid conditions. Yet, different from extensive research on the parameters tuning of controllers implemented at the turbine level, less attention can be found on the design of the PPC, as well as how to coordinate the PPC and the turbine level control to further improve the stability and dynamic performance of the WPP [19].

To tackle this challenge, this article proposes a complete control solution (including the PPC and turbine level control) for operating WPP under the weak grid conditions. It is pointed out that the better stability performance of the WPP can be guaranteed by implementing its voltage control at the bus with the highest $\partial Q/\partial V$. Hence, the centralized voltage control used in PPC is preferred over the decentralized voltage control adopted at the turbine level. Yet, the WPP would suffer from the poor disturbance rejection capability due to the slow dynamics of the PPC. Hence, a turbine-level dynamic voltage control is further added to improve the disturbance rejection capability of the WPP as well as its dynamic robustness against grid strength variations. Finally, simulation and field test results are given to demonstrate the theoretical analysis and the effectiveness of the proposed control method.

II. System Description

Fig. 1(a) shows the typical configuration of the WPP, where multiple WTs are connected to the ac system through step-up transformers and submarine cables. In the following analysis, the typical Type-IV WTs are assumed to be adopted in the WPP. When analyzing the dynamic interaction between WTs and the ac grid, the generator and machine-side converter (MSC) of the WT are usually ignored due to their limited impact [20], and only the grid-side converter (GSC) is of concern, whose control diagram is given in Fig. 1(b) [21]. By adopting the typical grid-following control, the GSC is synchronized with the power grid by means of the PLL. The CC loop is used to regulate the output current of the GSC (i_{WT}) to follow the current references (i_{dref} and i_{qref}) generated by DVC and reactive power control (RPC). P_{WT} and Q_{WT} are the active and reactive power output of the GSC, respectively.

Fig. 2 shows the equivalent circuit of the WPP-grid system, where WPP is modeled as an aggregated PQ source [3]. P_{gen}/Q_{gen} are output active/reactive power of the WPP, respectively, i.e., $P_{gen} = \Sigma P_{WT}$ and $Q_{gen} = \Sigma Q_{WT}$. R_{th}+jX_{th} represents the equivalent line impedance seen from the WPP. V and V_{th} represent RMS values of line-to-line voltages at Bus A and Bus B, respectively. θ denotes the voltage angle differences between these two buses, which is defined as power angle hereafter. An optional load with active power consumption P_{load} and a synchronous condenser (SynCon) with reactive power exchange Q_{SynCon} are also considered at Bus A to illustrate the effect of loading and reactive power compensation of the grid.

The active and reactive power (P and Q) transferred from Buses A to B can be expressed as follows [22]:

$$P = \alpha\left(V^2 - VV_{th}\cos\theta\right) + \beta VV_{th}\sin\theta \quad (1)$$

$$Q = \beta\left(V^2 - VV_{th}\cos\theta\right) - \alpha VV_{th}\sin\theta \quad (2)$$

where

$$\alpha = \frac{R_{th}}{|Z_{th}|^2} \tag{3}$$

$$\beta = \frac{X_{th}}{|Z_{th}|^2} \tag{4}$$

$$|Z_{th}| = \sqrt{R_{th}^2 + X_{th}^2}. \tag{5}$$

By eliminating θ from (1) and (2), the relationship between P and Q can be further derived as follows:

$$\left(P - \alpha V^2\right)^2 + \left(Q - \beta V^2\right)^2 = \left(\frac{V_{th}V}{|Z_{th}|}\right)^2 \tag{6}$$

which forms a circle with center (αV^2, βV^2) and radius $V_{th}V/|Z_{th}|$.

For the inductive transmission line that $X_{th} >> R_{th}$, (1) and (2) can be simplified as follows:

$$P = \frac{VV_{th}\sin\theta}{X_{th}} \tag{7}$$

$$Q = \frac{V^2 - VV_{th}\cos\theta}{X_{th}}. \tag{8}$$

III. Power Transfer Limit of WPP

A. Angle Stability Limit

It is well-known that the critical power angle at which the angle stability limit is reached can be calculated by solving $\partial P/\partial\theta = 0$ [4]. Based on (1), we have

$$\frac{\partial P}{\partial \theta} = VV_{th}\left(\alpha\sin\theta + \beta\cos\theta\right). \tag{9}$$

Solving $\partial P/\partial\theta = 0$ from (9), which yields

$$\theta_{\max\_Ang} = 90^\circ + \arctan\frac{R_{th}}{X_{th}}. \tag{10}$$

Substituting (10) into (1), which yields

$$P_{\max\_Ang} = \frac{1}{|Z_{th}|}\left(\frac{R_{th}}{|Z_{th}|}V^2 + VV_{th}\right). \tag{11}$$

Equation (11) illustrates the maximum power transfer capability of the system considering the angle stability limit. Define P_{norm} as the nominal power of the WPP, and then the per-unit (p.u.) representation of (11) is given by

$$P_{\max\_Ang\_\mathrm{pu}} = \frac{P_{\max\_Ang}}{P_{norm}} = \frac{1}{|Z_{th}|\,P_{norm}}\left(\frac{R_{th}}{|Z_{th}|}V^2 + VV_{th}\right). \tag{12}$$

The SCR is defined as the ratio between the short-circuit power from the ac system (S_{SC}) and the rated power of the WPP [3], i.e.,

$$SCR = \frac{S_{SC}}{P_{norm}}. \tag{13}$$

Without the local SynCon, it is known from Fig. 2 that S_{SC} can be calculated as follows:

$$S_{SC} = \frac{V_{norm}^2}{|Z_{th}|} \tag{14}$$

where V_{norm} represents the nominal voltage. Substituting (13) and (14) into (12), the relationship between $P_{\max\_Ang\_\mathrm{pu}}$ and SCR can be derived as follows:

$$P_{\max\_Ang\_\mathrm{pu}} = SCR\cdot\left(\frac{R_{th\_pu}}{|Z_{th\_pu}|}V_{pu}^2 + V_{pu}V_{th\_pu}\right). \tag{15}$$

It is known from (15) that larger R_{th} (lower X/R ratio) and higher V and V_{th} could improve the active power transfer capability. For the special case that $V = V_{th} = 1$ p.u. and $R_{th} = 0$, $P_{\max\_Ang\_\mathrm{pu}} = \mathrm{SCR}$ is yielded [11].

The above-mentioned conclusions can be visualized by the PQ curve that is plotted based on (6) with parameters X/R = 3, SCR = 1.2, $V_{th} = 1$ p.u., as shown in Fig. 3 (unless otherwise mentioned, only the part with $P \geq 0$ is plotted since WPP can only generate active power). It can be seen that $P_{\max\_Ang\_\mathrm{pu}}$ is around 1.6 p.u. with $V = 1$ p.u., which is larger than the SCR due to the presence of R_{th} in the transmission line. Moreover, it can also be observed that $P_{\max\_Ang\_\mathrm{pu}}$ can be increased (from around 1.5 to 1.7 p.u.) by boosting V (from 0.95 to 1.05 p.u.)

B. Voltage Stability Limit

By adopting the grid-following control, the ac voltage of the WPP is maintained by regulating the reactive power of each WT. Hence, $\partial Q/\partial V > 0$ is mandatory for guaranteeing the voltage stability of the system [5].

Based on (6), the relationship between Q and V can be expressed as follows:

$$Q = \beta V^2 - \sqrt{\frac{V_{th}^2V^2}{|Z_{th}|^2} - (P^2 - 2P\alpha V^2 + \alpha^2V^4)}. \tag{16}$$

Differentiating (16) in respect to V, which yields [23]

$$\frac{\partial Q}{\partial V} = 2\beta V - \frac{\frac{V_{th}^2V}{|Z_{th}|^2} + 2P\alpha V - 2\alpha^2V^3}{\sqrt{\frac{V_{th}^2V^2}{|Z_{th}|^2} - (P^2 - 2P\alpha V^2 + \alpha^2V^4)}}. \tag{17}$$

The p.u. representation of (17) can be calculated, which is given as (18) shown at the bottom of the next page.

If R_{th} is neglected, (18) can be simplified as follows:

$$\frac{\partial Q_{pu}}{\partial V_{pu}} = \frac{1}{X_{th\_pu}}\cdot\left(2V_{pu} - \frac{V_{th\_pu}}{\sqrt{1 - \frac{P_{pu}^2X_{th\_pu}^2}{V_{th\_pu}^2V_{pu}^2}}}\right). \tag{19}$$

Substituting (7), (13), and (14) into (19), the relationship between $\partial Q/\partial V$ and power angle θ can be expressed as follows:

$$\begin{aligned}\frac{\partial Q_{pu}}{\partial V_{pu}} &= \frac{1}{X_{th\_pu}}\cdot\left(2V_{pu} - \frac{V_{th\_pu}}{\sqrt{1-\sin^2\theta}}\right)\\ &= SCR\cdot\left(2V_{pu} - \frac{V_{th\_pu}}{\sqrt{1-\sin^2\theta}}\right).\end{aligned} \tag{20}$$

For the condition $V = V_{th} = 1$ p.u., it is known from (20) that $\partial Q/\partial V = \mathrm{SCR}$ when $\theta = 0^\circ$ (i.e., zero active power transfer).

Yet, $\partial Q/\partial V$ is reduced with the increased θ (i.e., increased active power transfer). A small $\partial Q/\partial V$ implies that a small amount of reactive power injection would result in a large voltage change at the point of connection of the WPP; which bring in challenges to the reactive power control. Moreover, this fast-changing voltage also imposes another challenge to the accurate phase angle tracking of the PLL.

The critical power angle where the voltage stability limit is reached ($\partial Q/\partial V = 0$) can be calculated as follows:

$$\frac{\partial Q_{pu}}{\partial V_{pu}} = 0 \Rightarrow \theta_{\max\_Vol} = \arcsin\sqrt{1-\left(\frac{V_{th\_pu}}{2V_{pu}}\right)^2}. \quad (21)$$

It can be calculated from (21) that $\theta_{\max\_\mathrm{Vol}} = 60°$ when $V = V_{th} = 1$ p.u., which is smaller than 90° power angle limit specified in (10). Hence, the voltage stability requirement imposes a stricter constraint on power transfer capability of the WPP than the angle stability requirement. This conclusion can be visualized by comparing Figs. 3 and 4(a) that is plotted based on (18), i.e., with X/R = 3, SCR = 1.2, $V = V_{th} = 1$ pu, the P_{max} of the WPP considering the angle stability limit is around 1.6 p.u. (see red dashed line in Fig. 3), but is reduced to around 1.2. p.u. when the voltage stability limit is considered, as shown by the black solid line in Fig. 4(a).

Moreover, it can also be clearly observed from (20) that the voltage stability is increased under the stiffer grid condition (larger SCR) and/or with higher sending end voltage (larger *V*), as shown in Fig. 4(a) and (b).

C. Impact of the Local Load

By considering the power consumption of the local load, it is known from Fig. 2 that the active power transferred from Buses A to B can be reduced as follows: $P = P_{gen}$ - P_{load}. This reduction of the active power transfer would lead to a better voltage stability of the system. As an example given in Fig. 4(b), with $P_{gen} = 1$ p.u. from the WPP, the active power delivered to the receiving end is reduced from 1 p.u. to 0.5 p.u. with 0.5 p.u. local load. It can be seen from the black solid line in Fig. 4(b) that $\partial Q/\partial V \approx 0.8$ when $P = 0.5$ p.u. and $V = 0.93$ p.u., and the WPP can work stably in this scenario. Yet, $P = P_{gen} = 1$ p.u. is yielded when there is no local load, and $\partial Q/\partial V$ is almost reduced to zero with $P = 1$ p.u. and $V = 0.93$ p.u. [see the black solid line in Fig. 4(b)]. Evidently, the WPP can hardly be stabilized under this operating condition.

It is worth mentioning that the SCR of the power grid is not affected by local loads at Bus A [see the definition of SCR from (13)]. Yet, the previous analysis has clearly demonstrated that the existence of local loads can increase the P_{max} of the WPP. Therefore, SCR-based P_{max} assessment would lead to too pessimistic result in the scenario with local loads. In a real power system, the load will be distributed on different locations of the grid, and the assessment is not as simple as in the illustration, but the general effect remains the same.

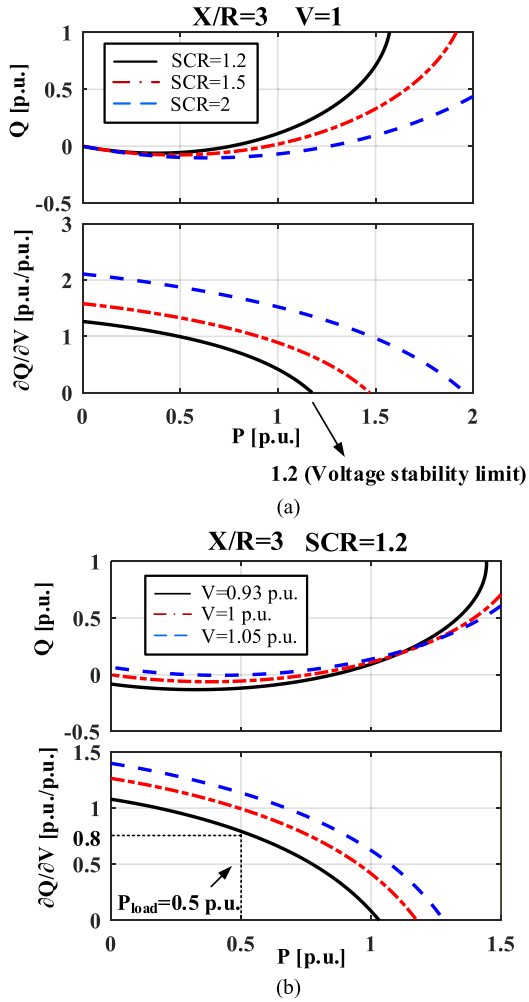

Fig. 4. *P-Q* and *P-*$\partial Q/\partial V$ curves of the system with X/R = 3, $V_{th} = 1$ p.u. (a) $V = 1$ p.u., with different SCR. (b) SCR = 1.2, with different sending end voltage V.

D. Impact of Synchronous Condenser

By considering a local SynCon, it is known from Fig. 2 that the reactive power generated from the WPP can be expressed as follows: $Q_{gen} = Q_{SynCon} + Q$, which yields

$$\frac{\partial Q_{gen\_pu}}{\partial V_{pu}} = \frac{\partial Q_{SynCon\_pu}}{\partial V_{pu}} + \frac{\partial Q_{pu}}{\partial V_{pu}}. \quad (22)$$

$$\frac{\partial Q_{pu}}{\partial V_{pu}} = \frac{1}{|Z_{th\_pu}|}\cdot\left(\frac{2X_{th\_pu}}{|Z_{th\_pu}|}V_{pu} - \frac{V_{th\_pu}^2 V_{pu} + 2P_{pu}R_{th\_pu}V_{pu} - 2\frac{R_{th\_pu}^2}{|Z_{th\_pu}|^2}V_{pu}^3}{\sqrt{V_{th\_pu}^2V_{pu}^2 - \left(P_{pu}^2|Z_{th\_pu}|^2 - 2P_{pu}R_{th\_pu}V_{pu}^2 + \frac{R_{th\_pu}^2}{|Z_{th\_pu}|^2}V_{pu}^4\right)}}\right). \quad (18)$$

By following the similar procedure given in (16)–(20), $\partial Q_{synCon\_pu}/\partial V_{\rm pu}$ can be calculated as follows:

$$\frac{\partial Q_{SynCon\_pu}}{\partial V_{pu}} = \frac{1}{X''_{d\_pu}}\left(2V_{pu} - \frac{V_{SynCon\_pu}}{\sqrt{1-\sin^2\delta}}\right) \quad (23)$$

where X''_{d_pu} and V_{SynCon_pu} are the subtransient reactance and the terminal voltage magnitude of the SynCon, respectively. δ represents the angle difference between voltages at Bus A and the terminal voltage of the SynCon. Since the SynCon does not generate nor absorb active power beyond the internal losses, $\delta \approx 0$ is yielded. Hence, (23) can be simplified as follows:

$$\frac{\partial Q_{SynCon\_pu}}{\partial V_{pu}} = \frac{1}{X''_{d\_pu}}\left(2V_{pu} - V_{SynCon\_pu}\right). \quad (24)$$

Substituting (20) and (24) into (22), which yields

$$\begin{aligned}\frac{\partial Q_{gen\_pu}}{\partial V_{pu}} &= \frac{1}{X''_{d\_pu}}\left(2V_{pu} - V_{SynCon\_pu}\right) \\ &\quad + \frac{1}{X_{th\_pu}}\left(2V_{pu} - \frac{V_{th\_pu}}{\sqrt{1-\sin^2\theta}}\right) \\ &= SCR_{SynCon}\left(2V_{pu} - V_{SynCon\_pu}\right) \\ &\quad + SCR_{th}\left(2V_{pu} - \frac{V_{th\_pu}}{\sqrt{1-\sin^2\theta}}\right) \end{aligned} \quad (25)$$

where SCR_{SynCon} and SCR_{th} represent the SCR contributed by SynCon and the grid, respectively. Based on the definition given in (13), the SCR at the connection point of the WPP by considering the impact of SynCon can be calculated as follows:

$$SCR = SCR_{SynCon} + SCR_{th}. \quad (26)$$

It is known from (25) that $\partial Q_{gen\_pu}/\partial V_{\rm pu}$ is increased by a constant factor SCR_{SynCon} by adopting SynCon (assume $V_{SynCon} = V_{th} = 1$ p.u.), which is visualized by comparing the $\partial Q_{gen\_pu}/\partial V_{\rm pu}$ curve with and without SynCon (red dashed and black solid line) in Fig. 5. Therefore, the critical power angle where the voltage stability limit is reached is increased by adding the SynCon in the sending bus. Nevertheless, the angle stability limit defined in (10) cannot be exceeded regardless the capacity of the added SynCon. Hence, the large transmission line impedance would still impose significant constraint on the P_{max} of the WPP, see (12).

Therefore, the improvement of the P_{max} of the WPP by adding local SynCon is usually not that significant compared to the case with the reduced transmission line impedance, even though they end up with the same SCR. As an example given by the red and blue lines in Fig. 5, with the same SCR = 2.2, the power transfer capability of the WPP with smaller transmission line impedance but no local SynCon ($\mathrm{SCR_{th}} = 2.2$, $\mathrm{SCR_{SynCon}} = 0$) is higher than that with larger transmission line impedance and local SynCon ($\mathrm{SCR_{th}} = 1.2$, $\mathrm{SCR_{SynCon}} = 1$).

E. Discussion

Based on previous analysis, it turns out that inaccurate P_{max} prediction might be yielded if the assessment is performed solely based on the value of SCR, as SCR itself cannot fully reflect the impact of operating voltage level, local loads, and other controlled units (like SynCon) on the P_{max} of the WPP; as shown in Figs. 4(b) and 5. In contrast, those impacts can be characterized by different values of $\partial Q/\partial V$. Therefore, the minimum $\partial Q/\partial V$, rather than minimum SCR, can be used as a metric for assessing P_{max} of the WPP with grid-following control. The value of minimum $\partial Q/\partial V$ can be calculated by the TSO based on max production and minimum load predictions.

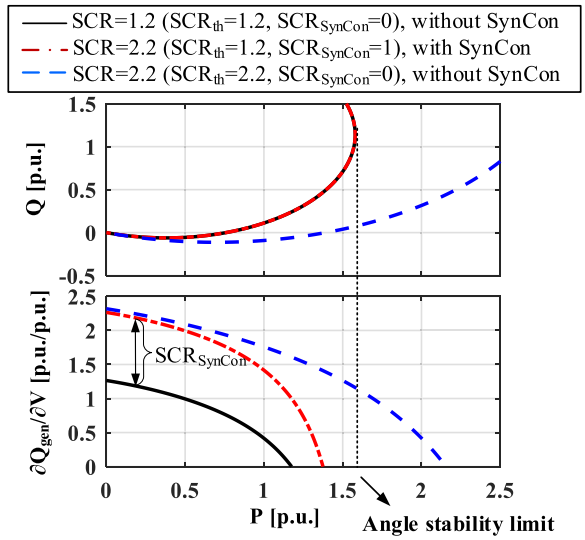

Fig. 5. *P-Q* and *P-*$\partial Q/\partial V$ curves of the system with or without SynCon. X/R = 3, $V = V_{th} = V_{SynCon} = 1$ p.u.

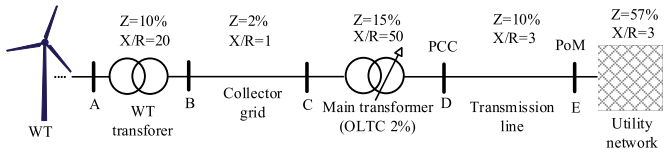

Fig. 6. Realistic aggregated representation of the WTs connected to the main grid.

TABLE I
SCR AND X/R VALUES FOR DIFFERENT BUSES

	Bus A	Bus B	Bus C	Bus D	Bus E
SCR	1.08	1.20	1.23	1.49	1.75
X/R	3.84	3.49	3.66	3	3

IV. Considerations of Controlling WPP Under the Weak Grid

A. Location of Implementing Voltage Control

Different from the simplified configuration given in Fig. 2, in practice the WT will be connected to the main grid through turbine transformer, collector network, main transformer, and transmission line, which forms multiple buses, e.g., Buses A–E shown in Fig. 6. The corresponding SCR and X/R values for different busses are given in Table I. It is worth mentioning that

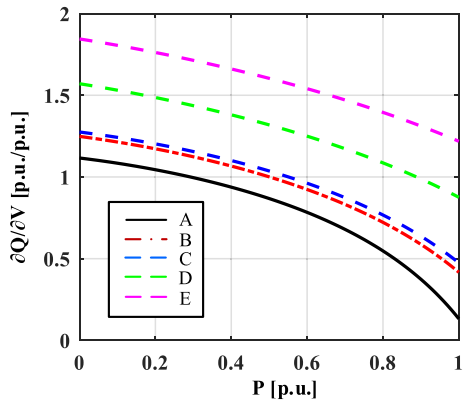

Fig. 7. *P*-$\partial Q/\partial V$ curves of different buses.

the SCR is calculated based on the nominal power of the WPP, and hence, its value is not affected by the number of turbines in the WPP.

Fig. 7 illustrates *P*-$\partial Q/\partial V$ curves for Buses A–E that is plotted based on (18) and the data from Table I. The highest $\partial Q/\partial V$ can be observed in Bus E due to the lowest grid impedance seen from this bus. Therefore, implementing voltage control at Bus E, rather than other buses, is preferred for enhancing the voltage stability and power transfer capability of the WPP.

B. Dynamic Voltage Control at Turbine Level

As pointed out in part A of this section, it is preferred to implement the voltage control at the point of measurement (PoM), i.e., Bus E, rather than turbine level (Bus A). Hence, the centralized voltage control is adopted in this article, which includes the PPC and the turbine controller, as shown in Fig. 8. V_{PoM}, Q_{PoM}, V_{PoMref}, Q_{PoMref} are voltage and reactive power at the PoM and their references, respectively. The PoM voltage is controlled by the PPC through dispatching reactive power setpoints (Q_{unite_set}) to different WTs. G_{V_plant} and G_{Q_plant} represent the voltage and reactive power controller used in PPC, respectively, and G_{del} represents the communication delay. The local reactive power control is implemented in turbine level to guarantee the output reactive power of each WT (Q_{unit}) to follow its reference (Q_{unite_ref}), where H_{conv} represents the closed-loop transfer function between Q_{unit} and Q_{unit_ref} Q_{dist} represents the reactive power disturbance. $\partial V_{PoM}/\partial Q_{PoM}$, $\partial V_{unit}/\partial Q_{unit1}$ represent the voltage sensitivity at the PoM and turbine terminal, respectively, which can be calculated based on the reciprocal of (18). Moreover, since the change of reactive power losses inside the WPP is neglectable during the disturbance, we have ΔQ_{PoM} (p.u.) $\approx \Delta Q_{unit1}$(p.u.). Hence, $\partial Q_{PoM}/\partial Q_{unit1} \approx 1$ is yielded with p.u. representation.

While the traditional centralized voltage control guarantees the good stability performance of the WPP under weak grid conditions, it suffers from the poor disturbance rejection capability, as the individual WT would not respond to the disturbance (e.g., switching event in the power grid) until the slow PPC changes Q_{unit_set}, which ends up with large voltage transients in the WPP.

To tackle this challenge, a turbine-level dynamic voltage controller (DynVC) is proposed in this work, as shown in Fig. 8, where K_v is the gain of DynVC. It can be seen that the DynVC is essentially a *Q*-*V* droop control that modifies Q_{unit_ref} based on turbine voltage V_{unit}. In order to guarantee Q_{unit} can still track Q_{unit_set} from the PPC during the steady-state operation, to limit frequent action of the transformer tap changer as well as avoiding hunting between turbines, the voltage reference of the DynVC (V_{unit_set}) is selected as the low-pass filtered voltage of the WT, such that the DynVC is only activated during the transient.

In the following analysis, the benefit of DynVC in improving the dynamic performance of the WPP will be elaborated. To analyze the response of the individual WT when subjecting grid disturbances, the transfer function between Q_{unit} and Q_{dist} can be derived based on Fig. 8, which is given in the following (the impact of the PPC is neglected here as its dynamics is much slower compared with that of the turbine-level control):

$$\frac{Q_{unit}}{Q_{dist}} = -\frac{sK_v\tau\frac{\partial V_{unit}}{\partial Q_{unit1}}H_{conv}}{1+s\tau\left(1+K_v\frac{\partial V_{unit}}{\partial Q_{unit1}}H_{conv}\right)} \tag{27}$$

where τ is the time constant of the low pass filter (LPF) used in DynVC, and its value is selected in the range of several seconds in practice. Therefore, $H_{conv}\approx 1$ can be assumed for the following analysis as its time constant is much smaller than τ.

It is clear that (27) is zero if DynVC is not used (i.e., $K_v = 0$), which means WT would not respond to the disturbance until the slow PPC changes Q_{unit_set}. On the other hand, (27) forms a high-pass filter by using DynVC ($K_v \neq 0$), indicating that the WT could respond to the disturbance in an instantaneous manner. Moreover, this instantaneous reactive power response (Q_{unit}) would counteract the effect of the disturbance (Q_{dist}), as highlighted by negative sign on the right-hand side of (27).

In order to investigate the overall dynamic performance of voltage control of the WPP with DynVC, the complete loop gain of the system considering both PPC and turbine-level control will be derived. It can be seen from Fig. 8 that the turbine-level control can be treated as the inner loop of the PPC, and its dynamics can be characterized by the closed-loop transfer function between Q_{unit_set} and Q_{unit1}, which is given by

$$H_{Q\_turbine} = \frac{Q_{unit1}}{Q_{unit\_set}} = \frac{1+\tau s}{1+\tau s\left(1+\frac{\partial V_{unit}}{\partial Q_{unit1}}K_v\right)}. \tag{28}$$

With (28), the complete voltage control scheme of the WPP given in Fig. 8 can be equivalent to that given in Fig. 9(a). Define H_{Q_plant} as the closed-loop transfer function between Q_{PoM_ref} and Q_{PoM}, which can be calculated based on Fig. 9(a) and is expressed as follows:

$$\begin{aligned} H_{Q\_plant} &= \frac{Q_{PoM}}{Q_{PoM\_ref}} \\ &= \frac{G_{Q\_plant}G_{del}H_{Q\_turbine}}{1+G_{Q\_plant}G_{del}H_{Q\_turbine}\frac{\partial Q_{PoM}}{\partial Q_{unit1}}}. \end{aligned} \tag{29}$$

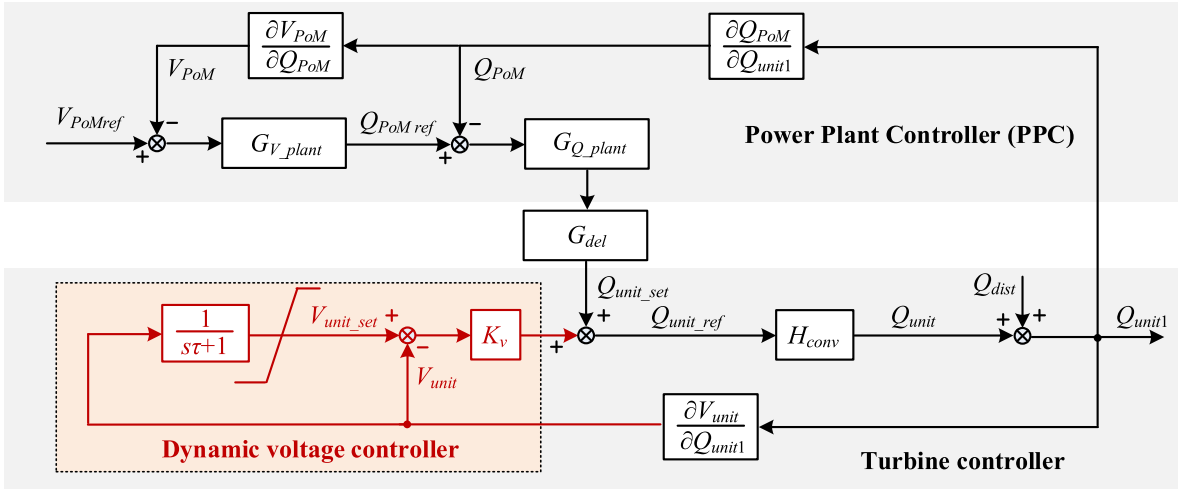

Fig. 8. Proposed voltage control scheme of the WPP: centralized voltage control + local dynamic voltage control.

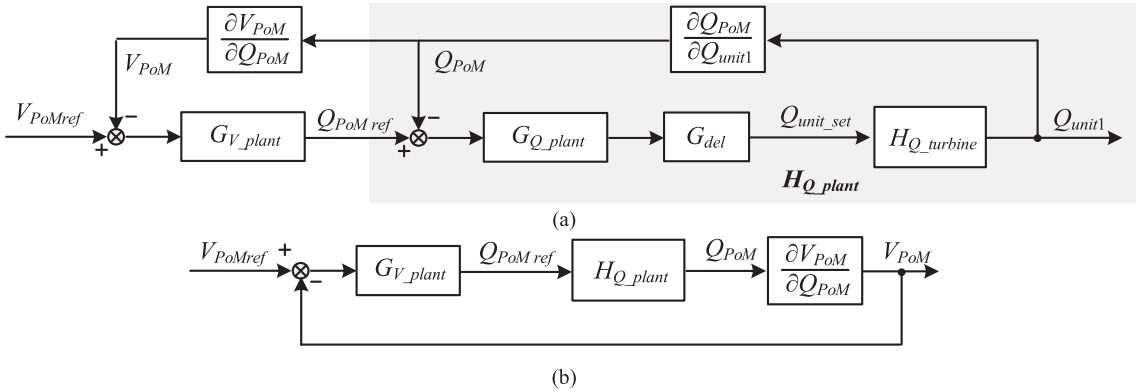

Fig. 9. Equivalent small signal representation of the proposed voltage control scheme of the WPP.

Then, Fig. 9(a) can be further equivalent to Fig. 9(b), with which, the complete open-loop gain of the WPP can be calculated as follows:

$$T_v = G_{v\_plant} H_{Q\_plant} \frac{\partial V_{PoM}}{\partial Q_{PoM}}. \tag{30}$$

Substituting (28) and (29) into (30), the final representation of the loop gain is given by

$$T_v = \frac{G_{v\_plant}\frac{\partial V_{PoM}}{\partial Q_{PoM}} G_{Q\_plant} G_{del}(1+\tau s)}{1+\tau s\left(1+\frac{\partial V_{unit}}{\partial Q_{unit1}} K_v + G_{Q\_plant} G_{del}\frac{\partial Q_{PoM}}{\partial Q_{unit1}}\right) + G_{Q\_plant} G_{del}\frac{\partial Q_{PoM}}{\partial Q_{unit1}}}. \tag{31}$$

It is noted that the DynVC introduces a $\partial V_{unit}/\partial Q_{unit1}$ term in the denominator of (31), which can partially counteract the effect of $\partial V_{PoM}/\partial Q_{PoM}$ in the numerator when subjected to the change of the SCR, since both $\partial V_{PoM}/\partial Q_{PoM}$ and $\partial V_{unit}/\partial Q_{unit1}$ will be increased under the weaker grid, and vice versa [see (18)]. Hence, by adopting the DynVC, the loop gain (dynamic performance of the WPP) becomes less sensitive to the variation of the grid strength.

The advantages of the proposed scheme can be summarized as follows:

- Good disturbance rejection capability such that the voltage variations of the WPP during the transient event can be reduced.
- Robust dynamics against variations of the grid strength.
- No hunting between turbines.
- Limited effect on tap changer operation.
- Possibility to gradually change between traditional centralized control and dynamic voltage control by changing K_v and τ.

V. Simulation and Real-Field Test Results

A. Verifications on Power Transfer Capability Prediction

Nonlinear time-domain simulations based on PSCAD/EMTDC are carried out to verify the $\partial Q/\partial V$ -based power transfer capability prediction in Section III. It should be emphasized that $\partial Q/\partial V > 0$ only indicates the WPP is operated within the physical constraint (voltage stability limit) imposed by the ac system, careful controller parameters tunning of the WPP is still needed to guarantee its stable operation.

1) Impact of Local Loads Under Same SCR: Fig. 10 shows the simulation results of the WPP connecting to the grid with

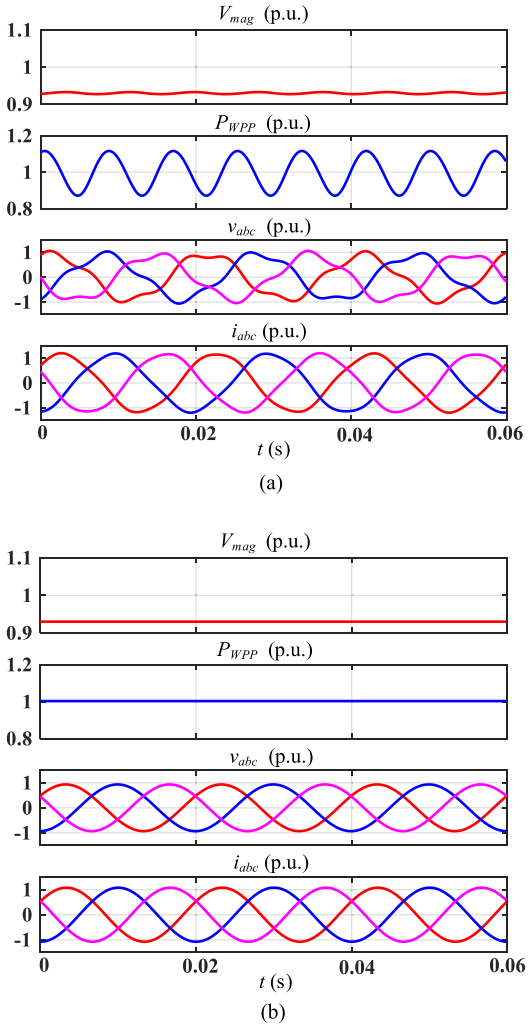

Fig. 10. Simulation results of the WPP connecting to the grid with SCR = 1.2, X/R = 3, $V_{\rm th} = 1$ p.u. and $V = 0.93$ p.u. (a) Without local load, unstable. (b) With 0.5 p.u. local load, stable.

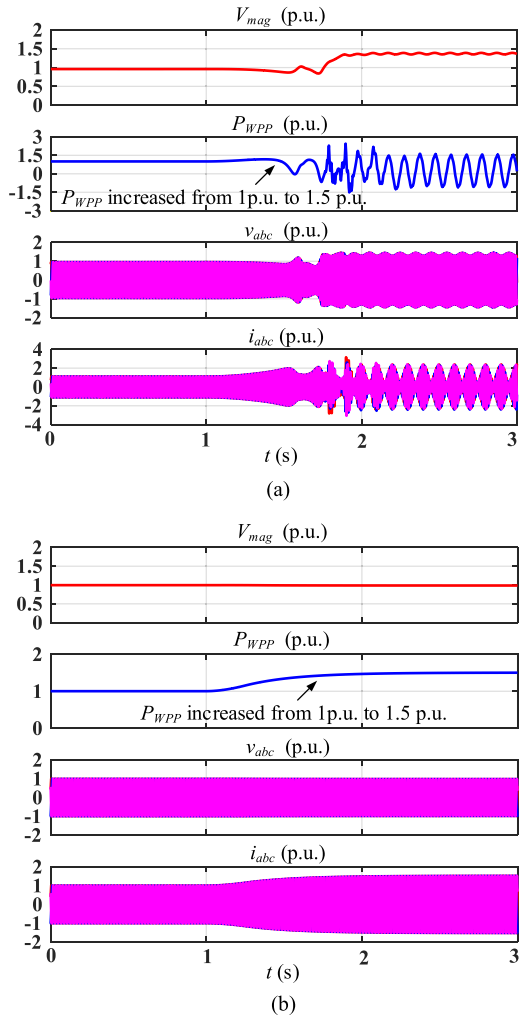

Fig. 11. Simulation results of the WPP connecting to the grid with SCR = 2.2, X/R = 3, $V_{\rm th} = 1$ p.u. and $V = 1$ p.u. (a) With larger transmission line impedance and local SynCon ($\text{SCR}_{\rm th} = 1.2$, $\text{SCR}_{\rm SynCon} = 1$), unstable. (b) With smaller transmission line impedance and no local SynCon ($\text{SCR}_{\rm th} = 2.2$, $\text{SCR}_{\rm SynCon} = 0$), stable.

SCR = 1.2, X/R = 3, $V_{th} = 1$ p.u. and $V = 0.93$ p.u. It can be seen from Fig. 10(a) that the WPP becomes unstable when generating 1 p.u. active power with the absence of local loads, due to the fact that $\partial Q/\partial V \approx 0$ predicted in Fig. 4(b). Yet, it is also known from Fig. 4(b) that $\partial Q/\partial V$ is increased to 0.8 when there is 0.5 p.u. local loads, and the WPP can work stably in this scenario, which is verified by simulation results given in Fig. 10(b). The simulation results given in Fig. 10 verify the power transfer capability predictions given in Fig. 4(b) considering the impact of local loads under the same SCR.

2) Impact of SynCon Under Same SCR: Fig. 11 shows the simulation results of the WPP connecting to the grid with SCR = 2.2. Two scenarios correspond to Fig. 5, i.e., with/without local SynCon, are considered. It can be seen from Fig. 11(a) that WPP becomes unstable when transferring 1.5 p.u. active power with larger transmission line impedance and local SynCon ($\text{SCR}_{\rm th} = 1.2$, $\text{SCR}_{\rm SynCon} = 1$), due to the negative $\partial Q/\partial V$ predicted by the red dash-dotted line in Fig. 5. Yet, the blue dashed line in Fig. 5 indicates $\partial Q/\partial V$ can be turned to positive at $P = 1.5$ p.u. if the transmission line impedance is reduced, even if local SynCon is not adopted ($\text{SCR}_{\rm th} = 2.2$, $\text{SCR}_{\rm SynCon} = 0$). The WPP can thus operate stably in this scenario, as demonstrated by simulation results given in Fig. 11(b).

It is worth mentioning that the motivation of simulating WPP with $P = 1.5$ p.u. is merely to validate the power transfer capability predicted in Fig. 5. In practice the WPP normally does not have the 1.5 p.u. overload capability due to the hardware limit.

B. Verifications of the Proposed Control Method

In order to verify the effectiveness of the proposed control method, field tests have been carried out on a real WPP. Due to the confidential requirement of the company, the elaboration of the test setup is not permitted, and all test results can only be presented after being per-unitized, as shown in Figs. 12 –14.

Fig. 12 shows the dynamic response of the WPP when subjecting to a sudden decrease of the SCR of the power grid (SCR is reduced from 20 to 1.5). It can be seen that the WPP can

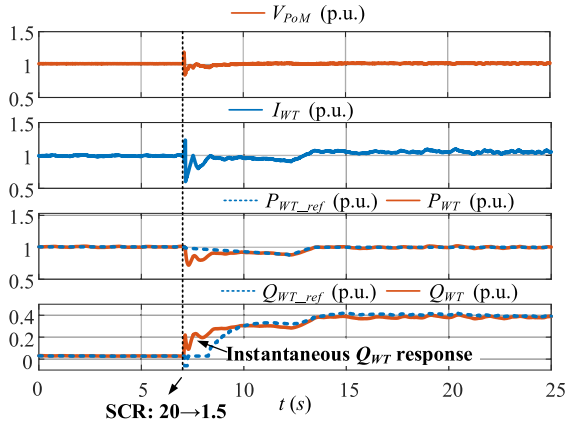

Fig. 12. Dynamic response of WPP under a sudden decrease of the SCR of the power grid (SCR is reduced from 20 to 1.5).

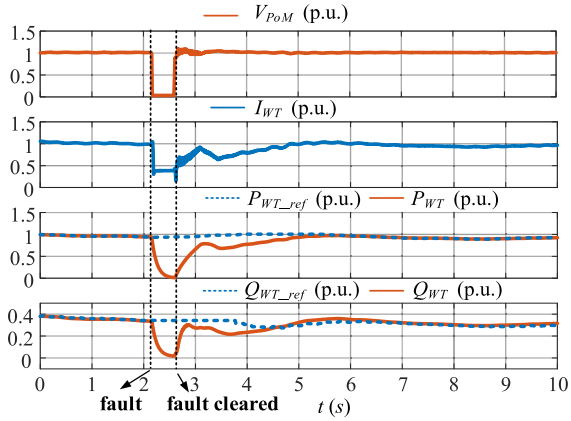

Fig. 13. Fault-ride through of the WPP under SCR = 1.5.

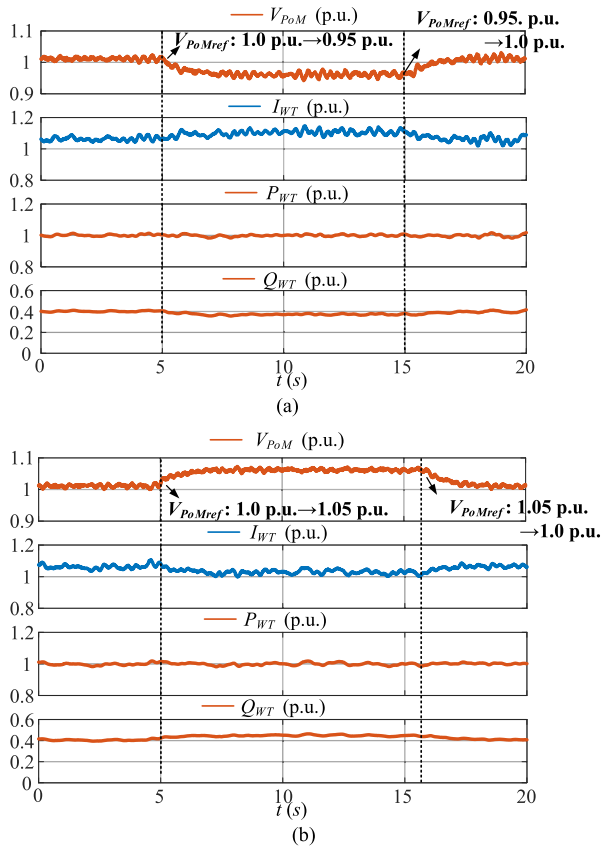

Fig. 14. Dynamic response of the WPP under the step change of V_{PoMref} with SCR = 1.5. (a) V_{PoMref}: 1.0 p.u. →0.95 p.u. → 1.0 p.u. (b) V_{PoMref} : 1.0 p.u. →1.05 p.u. → 1.0 p.u.

TABLE II
MAXIMUM AND MINIMUM STEADY-STATE VALUES OF V_{PoM} IN RESPECT TO DIFFERENT V_{PoMREF}

V_{PoMref} (p.u.)	V_{PoMmax} (p.u.)	V_{PoMmin} (p.u.)	(V_{PoMmax} - V_{PoMref})/V_{PoMref}	(V_{PoMmin} - V_{PoMref})/V_{PoMref}
0.95	0.9784	0.9423	+2.9%	–0.8%
1.0	1.0270	0.9876	+2.7%	–1.2%
1.05	1.0699	1.0512	+1.9%	+0.1%

work stably under the weak grid (SCR = 1.5) with the proposed control method that implementing the voltage control at the bus with the highest $\partial Q/\partial V$. Moreover, thanks to the proposed turbine-level DynVC, the output reactive power of the individual WT increases at the instant of SCR drops, rather than following the slowly increased reactive power command ($Q_{WT\cdot ref}$) from the PPC, as shown in Fig. 12. This fast reactive power response from the WT helps to reduce transients in PoM voltage (V_{PoM}) during grid disturbances.

Fig. 13 shows the dynamic response of the WPP under the grid fault, during which V_{PoM} is dropped to almost 0 p.u. It can be observed that the WPP with the proposed control method can successfully ride through the grid fault, and the active and reactive output power of the WT can be recovered to follow their commands after the fault clearance.

Fig. 14 shows the dynamic response of the WPP under the step change of voltage command of the PPC (V_{PoMref}), i.e., V_{PoMref} is reduced to 0.95 p.u. and then recovered to 1 p.u. in Fig. 14(a), while V_{PoMref} is increased to 1.05 p.u. and then recovered to 1 p.u. in Fig. 14(b). Table II further lists the maximum and minimum steady-state values of V_{PoM} in respect to different V_{PoMref}. It can be seen that the voltage fluctuation is less than $\pm 3\%$ of V_{PoMref}, which demonstrates that the WPP is capable of regulating V_{PoM} to follow V_{PoMref} in an accurate manner. Hence, the proposed turbine-level DynVC would not affect the voltage control accuracy at the plant level.

To further demonstrate the coordinated performance of different WTs with the proposed DynVC. A WPP with 25 turbines is simulated in PSCAD under a sudden decrease of SCR (from 20 to 1.5). It is worth mentioning that the control codes used in real PPC and turbine control are compiled to the dynamic link library (DLL) files and integrated into the PSCAD simulation environment, such that the simulation results could be very closed to that in the real field [24]. Fig. 15(a) shows the voltage, active and reactive power at the PoM, while the dynamics responses of different WTs are given in Fig. 15(b)–(d) (due to the page limit, only the results of 3 WTs are given).

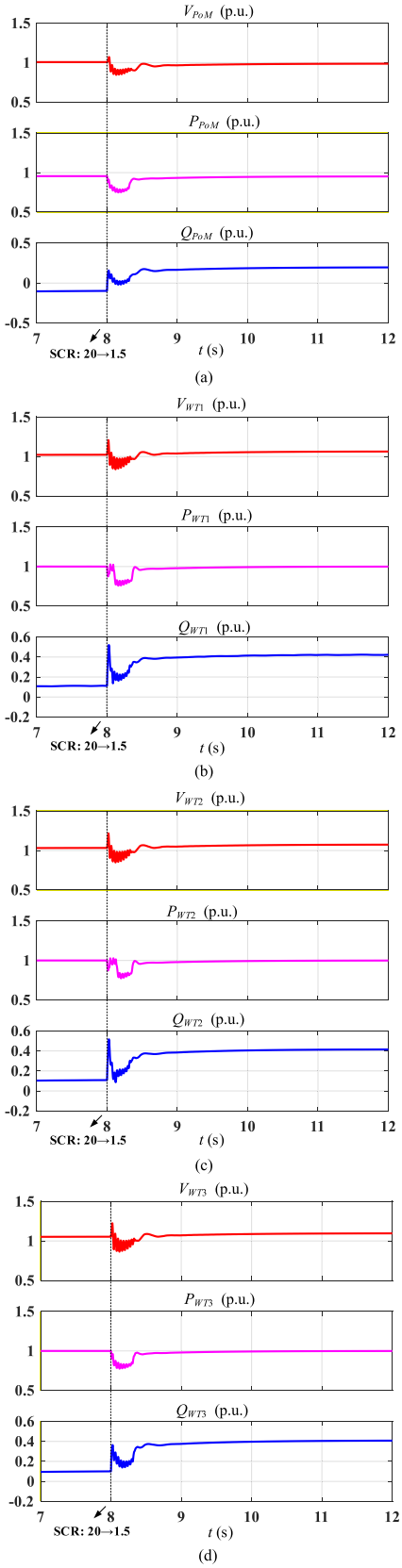

Fig. 15. Simulated response of the WPP under a sudden decrease of the SCR of the power grid (SCR is reduced from 20 to 1.5). (a) Voltage, active, and reactive power at the PoM. (b) Voltage, active, and reactive power of WT1. (c) Voltage, active, and reactive power of WT2. (d) Voltage, active, and reactive power of the WT3.

It can be seen that with the proposed DynVC, individual WTs increase their output reactive power in a coordinated manner to maintain the PoM voltage when subjecting to a sudden decrease of the SCR, and there is no hunting between different WTs.

VI. Conclusion

This article points out that the minimum $\partial Q/\partial V$ is a more appropriate metric for assessing the power transfer capability of the WPP compared with the minimum SCR. For operating the WPP under the weak grid condition, the centralized voltage control that controlling the voltage at the PoM is preferred due to its high $\partial Q/\partial V$. On top of this, a turbine-level dynamic voltage control is further added to improve the disturbance rejection capability of the WPP as well as its dynamic robustness against grid strength variations. Simulation and field test results are given to demonstrate the effectiveness of the proposed control method.

References

[1] S. Huang, J. Schmall, J. Conto, J. Adams, Y. Zhang, and C. Carter, "Voltage control challenges on weak grids with high penetration of wind generation: ERCOT experience," in *Proc. IEEE PES Gen. Meeting*, 2012, pp. 1–7.

[2] B. Badrzadeh et al., "Operational manifestation of low system strength conditions - Australian Experience," Tech. Rep. Cigre Session 2020 C2-124. [Online]. Available: https://e-cigre.org/publication/session2020-2020-cigre-session

[3] Cigre Working Group B4.62. TB 671, "Connection of wind farms to weak AC networks," Tech. Rep. 671, Cigre, 2016.

[4] P. Kundur, *Power System Stability and Control*. New York, NY, USA: McGraw-Hill, 1994.

[5] T. Cutsem and T. Vournas, *Voltage Stability of Electric Power Systems*. New York, NY, USA: Springer, 2005.

[6] NERC Reliability Guideline, *Integrating Inverter-Based Resources Into Low Short Circuit Strength Systems*, Atlanta, GA, USA: NERC, Dec. 2017. [Online]. Available: www.nerc.com

[7] NERC White Paper, *Short-Circuit Modeling and System Strength*, Atlanta, GA, USA: NERC, Feb. 2018. [Online]. Available: www.nerc.com

[8] Australian Energy Market Operator Limited (AEMO), *System Strength in the NEM Explained*, Melbourne, Australia: AEMO, Mar. 2020. [Online]. Available: https://aemo.com.au/-/media/files/electricity/nem/system-strength-explained.pdf

[9] Y. Zhang and A. M. Gole, "Quantifying the contribution of dynamic reactive power compensators on system strength at LCC-HVdc converter terminals," *IEEE Trans. Power Del.*, vol. 37, no. 1, pp. 449–457, Feb. 2022.

[10] J. Matevosyan, "Weak grid experiences in ERCOT," Presented in Western Electricity Coordinating Council (WECC) workshop, Oct. 2021. [Online]. Available: https://www.esig.energy/download/wecc-workshop-weak-grid-experiences-in-ercot-julia-matevosyan/

[11] J. Z. Zhou and A. M. Gole, "VSC transmission limitations imposed by AC system strength and AC impedance characteristics," in *Proc. 10th Int. Conf. AC DC Power Transmiss.*, Dec. 2012.

[12] S. Achilles, "Weak grid connection of IBR, why are we still talking about this?" Presented in G-PST/ESIG Webinar, Nov. 2021. [Online]. Available: https://www.esig.energy/event/g-pst-esig-webinar-series-weak-grid-connection-of-ibr-why-are-we-still-talking-about-this/

[13] J. Fortmann, M. Wilch, F. W. Koch, and I. Erlich, "A novel centralized wind farm controller utilizing voltage control capability of wind turbines," in *Proc. Power Syst. Comput. Conf.*, 2008, pp. 914–919.

[14] Y. Zhou, D. D. Nguyen, P. C. Kjær, and S. Saylors, "Connecting wind power plant with weak grid - challenges and solutions," in *Proc. IEEE PES Gen. Meeting*, 2013, pp. 1–7.

[15] A. J. Agbemuko, J. L. Dominguez-Garcia, O. Gomis-Bellmunt, and L. Harnefors, "Passivity-based analysis and performance enhancement of a vector controlled VSC connected to a weak AC grid," *IEEE Trans. Power Del.*, vol. 36, no. 1, pp. 156–167, Feb. 2021.

[16] X. Wang, L. Harnefors, and F. Blaabjerg, "Unified impedance model of grid-connected voltage-source converters," *IEEE Trans. Power Electron.*, vol. 33, no. 2, pp. 1775–1787, Feb. 2018.

[17] J. Zhou, D. Hui, S. Fan, Y. Zhang, and A. M. Gole, "Impact of short circuit ratio and phase-locked-loop parameters on the small-signal behavior of a VSC-HVdc converter," *IEEE Trans. Power Del.*, vol. 29, no. 5, pp. 2287–2296, Oct. 2014.
[18] H. Gong, X. Wang, and L. Harnefors, "Rethinking current controller design for PLL-synchronized VSCs in weak grids," *IEEE Trans. Power Electron.*, vol. 37, no. 2, pp. 1369–1381, Feb. 2022.
[19] J. Martínez, P. C. Kjær, P. Rodriguez, and R. Teodorescu, "Comparison of two voltage control strategies for a wind power plant," in *Proc. IEEE/PES Power Syst. Conf. Expo.*, 2011, pp. 1–9.
[20] M. Taul, X. Wang, P. Davari, and F. Blaabjerg, "An overview of assessment methods for synchronization stability of grid-connected converters under severe symmetrical grid faults," *IEEE Trans. Power Electron.*, vol. 34, no. 10, pp. 9655–9670, Oct. 2019.
[21] X. Wang, M. G. Taul, H. Wu, Y. Liao, F. Blaabjerg, and L. Harnefors, "Grid-synchronization stability of converter-based resources—An overview," *IEEE Open J. Ind. Appl.*, vol. 1, pp. 115–134, Sep. 2020.
[22] Y. W. Li and C.-N. Kao, "An accurate power control strategy for power electronics-interfaced distributed generation units operating in a low voltage multibus microgrid," *IEEE Trans. Power Electron.*, vol. 24, no. 12, pp. 2977–2988, Dec. 2009.
[23] T. Lund., "Analysis of distribution systems with a high penetration of distributed generation," Ph.D. dissertation, Ørsted, Tech. Univ. of Denmark, Kgs. Lyngby, Denmark, 2007.
[24] M. A. Cova Acosta et al., "Wind power plant modelling benchmark of RMS vs EMT simulation models for the electric reliability council of Texas (ERCOT) market," in *Proc. 20th Int. Workshop Large-Scale Integration Wind Power Power Syst. Well Transmiss. Netw. Offshore Wind Power Plants*, 2021, pp. 503–508.

Torsten Lund received the M.Sc. and Ph.D. degrees from Technical University of Denmark, Kgs. Lyngby, Denmark, in 2001 and 2007, respectively.

From 2001 to 2004, he worked for Siemens Automation and Drives in Germany, developing converter control software for electrical trains. From 2007 to 2015, he worked for the Danish TSO, Energinet, first as a Grid Planner, and finally as the Head of the department, Control Systems and Automation, developing solutions for the SCADA and EMS systems used in the daily operation of the power system. Since 2015, he has been with Vestas Wind Systems, Aarhus, Denmark, where he started Senior Specialist in the field of converter control and is currently the Chief Specialist with the overall design accountability of the PPC, electrical models, electrical balance of plant, and environmental protection. As subject matter expert for grid connection, he has been involved in the assessment grid connection of wind power plants in weak grids worldwide.

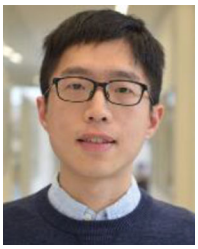

Heng Wu (Member, IEEE) received the B.S. and M.S. degrees in electrical engineering from Nanjing University of Aeronautics and Astronautics, Nanjing, China, in 2012 and 2015, respectively, and the Ph.D. degree in electrical engineering from Aalborg University, Aalborg, Denmark, in 2020.

He is currently an Assistant Professor with AAU Energy, Aalborg University. From 2015 to 2017, he was an Electrical Engineer with NR Electric Co., Ltd., Nanjing, China. He was a Guest Researcher with Ørsted Wind Power, Fredericia, Denmark, in 2018, and Bundeswehr University Munich, Germany, in 2019. From 2020 to 2021, he was a Postdoctoral Researcher with Aalborg University. He is the Co-Chair of IEEE Task Force on Frequency-domain Modeling and Dynamic Analysis of HVdc and FACTS, the Member of the technical committee (TC) of European Academy of Wind Energy (EAWE), the Member of GB grid forming best practice expert group formed by national grid ESO, U.K., the Member of Cigre working group B4.85 and B4/C4.93, and the Steering Committee Member of Cigre next generation network (NGN), Denmark. His research interests include the modeling and stability analysis of the power electronic based power systems.

Dr. Wu has been identified as the world's top 2% scientist by Stanford University since 2019. He received the 2019 Outstanding Reviewer Award for the IEEE TRANSACTIONS ON POWER ELECTRONICS and the 2021 Star Reviewer Award for the IEEE JOURNAL OF EMERGING AND SELECTED TOPICS IN POWER ELECTRONICS.

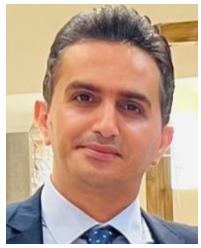

Hamid Soltani (Member, IEEE) received the B.Sc. and M.Sc. degrees in electrical engineering from the University of Mazandaran (Noushirvani), Babol, Iran, in 2005 and 2008, respectively, and the Ph.D. degree in power electronics from Aalborg University, Aalborg, Denmark, in 2016.

From 2009 to 2013, he was with the Department of Electrical and Computer Engineering, Golestan University, Gorgan, Iran, as a Lecturer. From May 2016 to June 2017, he was with the Department of Energy Technology, Aalborg University, as a Postdoctoral Researcher working on new generation of adjustable speed drives. In June 2017, he joined the Department of Converter Control, Vestas Wind Systems A/S, Aarhus, Denmark, and worked on grid performance and integration of turbines toward wind power plant until October 2021. He is currently a Lead Engineer with the power plant Integration department in Vestas, mainly focusing on weak grids and stability of the turbines and the power plants. His research interests include modeling and stability analysis of power electronic based power systems.

John Godsk Nielsen was born in 1972. He received the M.S. degree in electrical engineering from Aalborg University Electrical Energy Technology, Aalborg, Denmark, in 1998, and the Ph.D. degree in electrical engineering from Aalborg University, Aalborg, Denmark, in 2002, with the area design and control of a dynamic voltage restorer for use in customized power systems.

From 2002 to 2022, he was an Electrical Engineer with Vestas Wind Systems, Denmark. Working within converter control and hardware design including control of electrical machines and focus on grid performance and integration of turbines toward wind power plant and grid requirements. His research interests include modeling and stability analysis of power electronic based power systems.

Gert Karmisholt Andersen received the M.Sc. degree from Aalborg University, Aalborg, Denmark, in 1998.

From 2002 to 2005, he worked as an Assistant Professor with the Institute of Energy Technology, Aalborg University, within the fields of modeling and control of power electronics. From 2005 to 2019, he worked with Vestas Wind Systems, Aarhus, Denmark, developing converter control software, where since 2019 he has been a Senior Specialist in the field of converter control.

Xiongfei Wang (Senior Member, IEEE) received the B.S. degree from Yanshan University, Qinhuangdao, China, in 2006, the M.S. degree from Harbin Institute of Technology, Harbin, China, in 2008, both in electrical engineering, and the Ph.D. degree in energy technology from Aalborg University, Aalborg, Denmark, in 2013.

Since 2009, he has been with the Department of Energy, Aalborg University (AAU Energy), where he became an Assistant Professor in 2014, an Associate Professor in 2016, and a Professor and a Leader of the Electronic Power Grid (eGRID) Research Group in 2018. Since 2020, he has also been a Part-Time Professor with KTH Royal Institute of Technology, Stockholm, Sweden. His current research interests include modeling and control of power electronic converters and systems, stability and power quality of power-electronics-dominated power systems, and high-power converters.

Dr. Wang serves as the Co-Editor-in-Chief for the IEEE TRANSACTIONS ON POWER ELECTRONICS and an Associate Editor for the IEEE JOURNAL OF EMERGING AND SELECTED TOPICS IN POWER ELECTRONICS. He has received 9 Prize Paper Awards in the IEEE transactions and conferences, the 2016 AAU Talent for Future Research Leaders, the 2018 Richard M. Bass Outstanding Young Power Electronics Engineer Award, the 2019 IEEE PELS Sustainable Energy Systems Technical Achievement Award, the 2020 IEEE PES Prize Paper Award, the 2020 JESTPE Star Associate Editor Award, the 2022 Isao Takahashi Power Electronics Award, and the Highly Cited Researcher in the Web of Science from 2019.